THE ASTROPHYSICAL JOURNAL, 424:333–344, 1994 March 20

COOL ZERO-METALLICITY STELLAR ATMOSPHERES

D. SAUMON,[1,2] P. BERGERON,[3] J. I. LUNINE,[2] W. B. HUBBARD,[2] AND A. BURROWS[4]

Received 1993 August 31; accepted 1993 September 22

ABSTRACT

Very low mass stars and brown dwarfs have low effective temperatures and their atmospheric opacities are provided by heavy elements which form a host of strongly absorbing molecules. We present a study of the atmospheres and emergent spectra of these objects in the limiting case of *zero metallicity*. A grid of atmosphere models is presented, based on updated opacities for H/He mixtures, in particular for the collision-induced absorption by H_2 which plays an important role in these atmospheres. The emergent spectra bear little resemblance to the corresponding blackbody emission and become *bluer* as the effective temperature is *lowered*. The atmosphere models are coupled with interior calculations to obtain accurate physical and photometric characteristics for the low-mass end of the zero-metallicity main sequence. This provides a useful boundary in the Hertzsprung-Russel diagram to interpret observations of low-metallicity stars.

Subject headings: stars: abundances — stars: atmospheres — stars: low-mass, brown dwarfs

1. INTRODUCTION

Comparisons between theoretical and observed spectra of very low mass (VLM) stars and brown dwarfs have largely focused on high-metallicity, essentially Population I objects (e.g., Kirkpatrick et al. 1993) because they are readily observable in the solar neighborhood and in young star clusters. However, disagreements between the theoretical models and observations, of increasing severity with decreasing effective temperature (Kui 1991), point out the difficulty of accurately including molecular lines (Allard 1990) and condensing grains in atmospheres with effective temperatures cooler than 2500 K (Lunine et al. 1993). Leggett (1992) has suggested that the portion of the underlying continuum opacity due to hydrogen and helium needs to be reexamined, in light of the substantial revisions to the collision-induced hydrogen opacity of Lenzuni, Chernoff, & Salpeter (1991).

While the contribution of this opacity source appears to be too small in Population I atmospheres to resolve the mismatch of the continuum spectra (Allard 1990), it is important in models of extreme Population II objects ($Z \lesssim 0.001\ Z_\odot$; Burrows et al. 1993), which might form the bulk of the Galactic halo, as suggested by the recent detection of gravitational microlensing events by halo objects (Alcock et al. 1993; Aubourg et al. 1993). Given a plausible age of halo members, direct detection of individual brown dwarfs in that population is essentially impossible (Burrows & Liebert 1993). However, hydrogen-burning halo objects are detectable, and Monet et al. (1992) observed low-metallicity subdwarfs with halo kinematics for which they estimated a mean metallicity of $Z = 0.02\ Z_\odot$, based on indirect evidence. Richer & Fahlman (1992) have studied the low-mass stellar population of the halo. Based on sample selection criteria, as well as kinematic and photometric data, they argue that the subdwarf sequence of Monet et al. (1992) must have a metallicity well below the average Population II value of $\approx 0.01\ Z_\odot$.

As shown below, the photometric colors of the VLM Population III objects are very different from those of later generation stars. From the point of view of interior modeling, an accurate computation of the atmospheric, or surface, boundary condition for such objects is not straightforward, due to the extremely low opacity of the envelope and onset of convection at low optical depths (Burrows et al. 1993). In this regime, great care must be taken to ensure proper flux conservation throughout the atmosphere to obtain a correct surface boundary condition for extreme Population II evolutionary models. Understanding the transition between such behavior and that of more normal, metal-rich stars in itself lends interesting insights into the accuracy of VLM star models, as well as into the interpretation of the observations of halo stars of VLM. The latter population could contribute a significant fraction of the galactic dark matter (Richer & Fahlman 1992), but this conclusion depends on the derived space density, which in turn depends sensitively on the accuracy of the physical models which determine the metallicity (Burrows & Liebert 1993).

This paper represents our initial effort to compute detailed nongray model atmospheres for VLM stars and brown dwarfs. Herein, we construct radiative-convective model atmospheres for zero-metallicity objects as one approach toward addressing the issues discussed above. The opacity associated with pure hydrogen-helium objects can be readily computed, making fully coupled atmosphere and interior models tractable. We computed a large grid of fully nongray atmospheric models to assess the errors associated with using gray atmosphere models for computing temperature profiles in extreme Population II objects and to predict the difference in appearance between Population I and extreme Population II objects when surveyed using spectra and broad-band photometry.

The present work also allows us to assess accurately the effect on the spectra of incorporating the new collision-induced hydrogen opacity of Lenzuni et al. (1991). We find that the new opacities have a dramatic effect on zero-metallicity spectra and should have an effect on extreme Population II spectra. Together with the Population I models of Burrows et al. (1993), computed using relatively crude gray opacities, we can use the

[1] Hubble Postdoctoral Fellow.
[2] Department of Planetary Sciences, University of Arizona, Tucson, AZ 85721; dsaumon, jlunine, hubbard@hindmost.lpl.arizona.edu.
[3] Département de Physique, Université de Montréal, C.P. 6128, Succ. A, Montréal, Québec, Canada, H3C 3J7; bergeron@astro.umontreal.ca.
[4] Departments of Physics and Astronomy, University of Arizona, Tucson, AZ 85721; burrows@arizrvax.bitnet.

models to bracket the evolution and spectra of stars as a function of metallicity.

The plan of the paper is as follows: § 2 describes the atmosphere code and the treatment of the input physics. The atmospheric structure of zero-metallicity objects is discussed in § 3. In § 4 we display detailed emergent spectra and present the broad-band colors for standard bandpasses. In § 5, the atmosphere models are coupled with evolutionary calculations and new, accurate results are given for the Population III main sequence.

2. MODEL ATMOSPHERE CALCULATIONS

In the absence of metals, the equation of state and the opacity of the stellar material are greatly simplified and it is relatively straightforward to set up the atmosphere calculation. We have used an atmosphere code originally developed for the calculation of white dwarf atmospheres. It is fully described in Bergeron (1988) and in Bergeron, Wesemael, & Fontaine (1991). The built-in assumptions include the plane-parallel approximation, constant gravity throughout the atmosphere and local thermodynamic equilibrium (LTE), all of which apply to VLM stars and brown dwarfs. For a given pressure and temperature structure, the radiative transfer equation is solved with the Feautrier method. The resulting variable Eddington factors are used in the fully linearized equations of stellar atmospheres which are solved for pressure and temperature corrections with the Rybicki solution. We have found that a simple temperature linearization of the equations converges to an identical atmospheric structure in most cases, with a much shorter execution time.

Convection is an important energy transport mechanism in these atmospheres, and it is included self-consistently in the equation of flux conservation and in the linearization procedure. We have adopted the phenomenological mixing-length formalism which accounts for radiative losses during the lifetime of a convective eddy. Alternate, nonlocal formulations of convective transport are now available (Canuto & Mazzitelli 1992; Lydon, Fox, & Sofia 1992 and references therein). While they involve no free parameters and are quite successful when applied to solar models, it is not yet possible to assess their validity in modeling qualitatively different types of stars. In this context, and despite its limitations, the mixing-length formulation remains a viable alternative.

The iteration procedure is considered to have converged to the atmospheric structure when the temperature and pressure corrections have become small enough: $\Delta T/T \leq 10^{-3}$ and $\Delta P/P \leq 10^{-2}$. In most models, corrections which are smaller than these limits by one or two orders of magnitude are easily achieved. In all cases, these convergence criteria lead to total flux conservation to an accuracy better than 1 part in 10^3 in each layer of the atmosphere. We have found that in models with very low effective temperature ($T_{\rm eff} \leq 1500$ K) and high gravity ($\log g \geq 4.5$), the convective flux is *extremely* sensitive to the temperature stratification of the atmosphere. Convergence of such models is very difficult to achieve and the iteration procedure oscillates. In such cases, a final structure with satisfactory flux conservation was obtained by gradually constraining the amplitude of the temperature corrections.

2.1. *The Equation of State*

Under the assumption of LTE, the equation of state of the H/He mixture depends only on T, P, and the helium mass fraction Y. We use an ideal gas (i.e., noninteracting) equation of state (EOS) which includes the following species: H_2, H, H^+, H^-, H_2^+, H_3^+, He, and e. The temperature is always below 8000 K and ionization of He is completely negligible. In a metal-free mixture, it is particularly important to include the molecular ions H_2^+ and H_3^+ because their presence affects the concentration of the H^- ion, a very important opacity source in these atmospheres. This point is made clearly in Figures 3–7 of Lenzuni et al. (1991).

The treatment of the bound states of these atomic and molecular species can affect strongly their concentrations at chemical equilibrium. For H and He, all internal states are included in the internal partition function sum up to a cutoff level determined by the mean interparticle distance. This rather crude cutoff procedure is justified by the relatively low temperatures of interest ($T < 8000$ K) where the degree of thermal excitation of H and He is very low. For H_2 and H_2^+, we have summed over all vibrational and rotational levels of the electronic ground state using the spectroscopic constants given by Huber & Herzberg (1979). The dissociation energy and the partition function of H_3^+ have recently been revised by Chandra, Gaur, & Pande (1991).

Because of the relatively low opacity of H/He mixtures at low temperatures, the zero-metallicity atmospheres are compact and dense (see § 3). In the coolest ($T_{\rm eff} \leq 1500$ K) and highest gravity ($\log g \geq 5$) atmospheres, pressures above 10^9 dyn cm^{-2} can be reached at large Rosseland mean optical depths ($\tau_R > 40$). A comparison between the ideal EOS used in this work and the EOS of Saumon & Chabrier (1992), which carefully accounts for nonideal effects, shows that the deviation between the two $\rho(T, P)$ relations is at most 15% under the conditions found in the lowest $T_{\rm eff}$, highest gravity atmospheres. The importance of nonideal effects decreases very rapidly to a level below 1% at lower optical depths. Because the nonideal effects become important only for a few extreme models, and then only at such large τ_R that they have no effect on the emergent spectrum, the use of an ideal EOS is justified.

2.2. *Opacity Sources*

In these atmospheres, the temperature remains too low to excite levels in H and He which lead to transitions in the wavelength range where the radiative flux is important. We have therefore neglected absorption lines of H and He in our description of the opacity. On the other hand, we have included all the important continuum opacity sources for mixtures of H and He. Tables 6 and 7 of Lenzuni et al. (1991) list the relevant scattering and absorption processes along with updated cross sections. We have found and corrected a minor error in the H_2^+ opacity used by Lenzuni et al. (1991) for which the correction for stimulated emission is missing. Since H_2^+ is a minor contributor to the opacity, this has negligible consequences.

The H_2 molecule has no permanent dipole moment and dipolar radiative transitions are therefore forbidden. At sufficiently high densities, however, collisions with neighboring H_2 molecules, as well as H and He atoms, induce temporary dipole moments in the molecule, thereby allowing dipole transitions. This is the so-called collision-induced absorption (CIA) by H_2, a very important source of opacity in zero-metallicity atmospheres. A good review of this absorption mechanism is given in Lenzuni et al. (1991) who have compiled the various contributions to H_2 CIA and devised some extensions to the existing quantum mechanical calculations. Their absorption cross sec-

tions, which we have used in this work, are based on the ab initio calculations of Borysow, Frommhold, & Moraldi (1989), Borysow & Frommhold (1989, 1990, and references therein). These recent calculations of the H_2 CIA represent a tremendous improvement in accuracy in band shapes and intensities over the pioneering work of Linsky (1969) and Patch (1971). Collision-induced absorption by H_2 is by far the most complicated and, until recently, the least well understood of the opacity sources relevant to zero-metallicity atmospheres. The calculation of a grid of reliable $Z = 0$, low-$T_{\rm eff}$ model atmospheres is made possible for the first time by these new cross sections.

After the completion of this work, an error was found in the cross section for the roto-translational band of the H_2–H_2 CIA spectrum of Lenzuni et al. (1991). This leads to an overestimate of the band intensity by up to a factor of 1.3 (Borysow 1993). Fortunately, this band is centered around 10 μm, where our emergent spectra show very little flux and the error becomes important only in regimes where other opacity sources contribute significantly in this wavelength range. Therefore, we do not expect any significant consequence on the computed atmospheric structures and emergent spectra.

The degree of ionization being always below 10^{-6}, the opacity is dominated by three sources: H_2 CIA, Rayleigh scattering by H_2 and H, and H^- bound-free and free-free absorptions. Figure 1 shows the frequency dependence of the total absorption coefficient in a model at $T_{\rm eff} = 3000$ K and log $g = 5$. Each curve represents a different depth in the atmosphere, from the surface at log $\tau_R = -6$ (*bottom curve*) to log $\tau_R = 2$ (*top curve*). The four absorption bands in the far-red and infrared are due to H_2 CIA. Throughout most of this model, Rayleigh scattering is the dominant opacity source in the visible part of the spectrum (with the characteristic ν^4 dependence) but it is replaced by the nearly flat H^- bound-free absorption deep in the atmosphere. Note that when H_2 CIA and Rayleigh scattering are the main opacity sources, a "window" is formed around $\nu = 1$ μm^{-1} where the opacity is minimal.

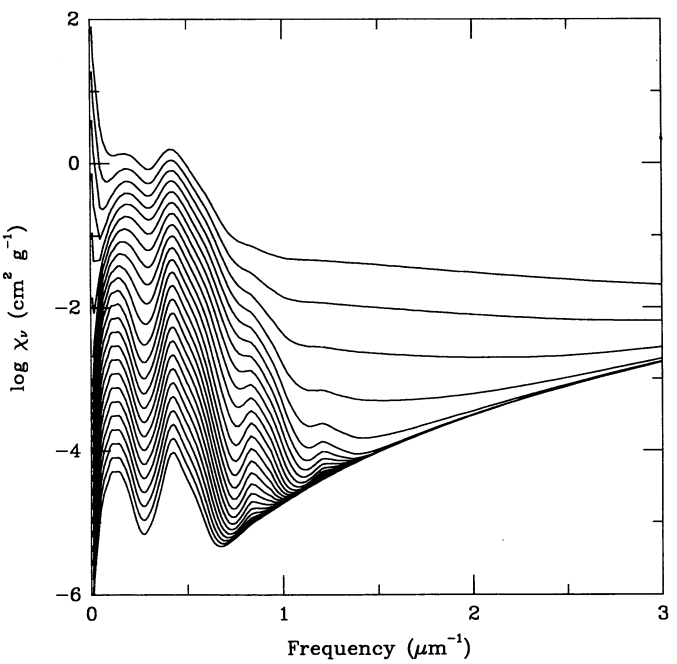

FIG. 1.—Frequency dependence of the total absorption coefficient. Each curve corresponds to a different depth in a $T_{\rm eff} = 3000$ K, log $g = 5$ atmosphere model ranging from log $\tau_R = -6$ (*bottom*) to log $\tau_R = 2$ (*top*) in steps of 0.33.

2.3. *A Discussion of Radiative Equilibrium*

The temperature structure of the optically thin part of the atmosphere ($\tau_R \ll 1$) is essentially determined by the equation of radiative equilibrium,

$$\int_0^\infty \kappa_\nu(P, T)[B_\nu(T) - J_\nu(P, T)]d\nu = 0 , \qquad (1)$$

where κ_ν is the true absorption coefficient (excluding scattering), B_ν is the blackbody function, and J_ν is the mean intensity of the radiation field at frequency ν. This equation, imposed for each radiative layer of the atmosphere model, expresses local energy conservation. Typically, T is nearly constant in a radiative zone in LTE when $\tau_R \ll 1$.

We have found that for all models where the optically thin radiative region enters the regime of molecular dissociation, a large discontinuity of several hundred degrees develops in the *converged* T structure. The affected models span the range of $3500 \lesssim T_{\rm eff} \lesssim 4500$ K, with a weak dependence on gravity. This discontinuity in T occurs at such low optical depth that the emergent spectrum is not affected at all. This situation is illustrated in Figure 2 which shows two converged models with $T_{\rm eff} = 3800$ K and log $g = 3.5$. The two different structures, shown by open and solid circles respectively, were obtained by starting the iterative solution from two different initial structures. Both solutions satisfy the equations of stellar atmospheres (hydrostatic equilibrium, radiative transfer, and radiative equilibrium) to a very high degree of accuracy. In addition, the emergent spectrum for these two models is very nearly identical: they depart from each other by $\Delta H_\nu/H_\nu(\max) < 4 \times 10^{-7}$. This is a consequence of the fact

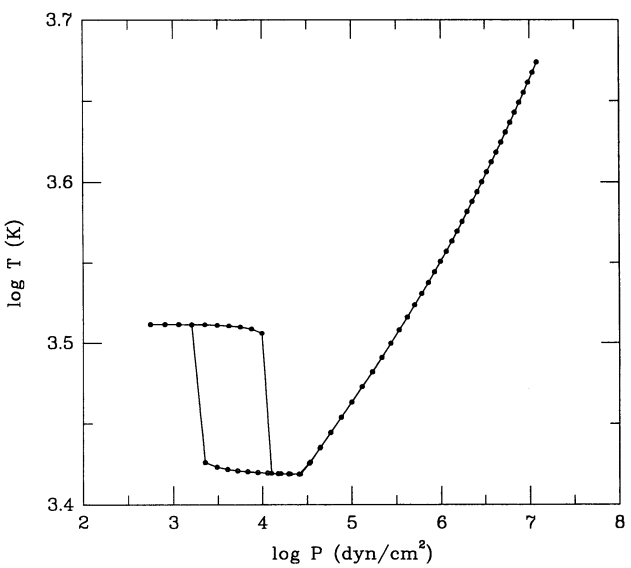

FIG. 2.—Atmosphere models with $T_{\rm eff} = 3800$ K and log $g = 3.5$. The two models are fully converged but were obtained from two different initial structures. Open and filled circles indicate the vertical zoning of each model which extend over $-6 < \log \tau_R < 2$. The sharp bend at log $P = 4.45$ signals the onset of convection. See text.

that the spectrum is formed at much greater depths than that of the discontinuity. A very detailed investigation of this problem has revealed that the discontinuity is *not* caused by (1) the small number of frequency points used in the quadrature, (2) the number or vertical distribution of the layers in the models, (3) discontinuous behavior of the EOS or opacity subroutines, (4) numerical inaccuracies in the calculation of the radiative field properties (J_ν in particular), or even (5) the numerical method to solve the equation of radiative equilibrium. Actually, we obtained the same anomalous results by applying the Λ-iteration method (Mihalas 1978, p. 179). After performing an extensive series of tests, we found that this abnormal solution is actually related to the behavior of the opacity over a narrow temperature range.

Molecular dissociation and the absence of electron-donor metals in this zero-metallicity calculation combine to create a peculiar behavior in κ_ν which to our knowledge has not been discussed before. At temperatures above the region of molecular dissociation, hydrogen is in atomic form and a small level of ionization provides electrons to form H^- which dominates κ_ν mostly in the visible and in the far-infrared. On the other hand, for T below the region of molecular dissociation, the absorption is provided only by H_2 CIA, which absorbs at infrared wavelengths, just in the minimum of the H^- opacity. In the intermediate regime of molecular dissociation, over a temperature range of a few hundred degrees, there are too few molecules to cause CIA and too few free electrons to form H^-. Consequently, κ_ν drops by about one order of magnitude over the whole frequency range of interest. In other words, as T is decreased and H atoms recombine to form molecules, κ_ν is initially large at visible wavelengths and small in the infrared, then very small over the whole frequency range of interest, and finally it rises again at near-infrared wavelengths only.

We have studied the behavior of the integral in equation (1) in the radiative zone of one of the pathological models. In these models, the radiative zone is well approximated by an isothermal $T(P)$ profile satisfying the equation of hydrostatic equilibrium. By systematically varying T in the radiative zone, all T-independent quantities being kept fixed, we found that equation (1) can have one or three distinct roots. There is also a degenerate case with only two distinct roots. The existence of multiple T solutions to equation (1) is undoubtedly caused by the peculiar behavior of κ_ν discussed above. The evolution of the roots as a function of depth in the atmosphere completely explains the observed discontinuity in the converged T structure. The multiplicity of the roots is reflected in the two converged temperature structures shown in Figure 2.

Note that such discontinuities do not appear in *gray* model atmospheres where κ_ν is replaced by its frequency-independent Rosseland mean, κ_R. In this case equation (1) simplifies to

$$\int_0^\infty [B_\nu(T) - J_\nu(P, T)]d\nu = B - J = 0 , \quad (2)$$

which is independent of the opacity.

It appears that for these models, very minute departures from radiative equilibrium (or flux conservation, $\Delta H/H < 10^{-6}$) drive T from one root to another, causing the discontinuity. Artificial removal of the discontinuity gives a model which still satisfies the flux conservation condition to better than one part in 10^4 and does not affect the emergent flux.

For models which enter the regime of molecular dissociation, we have used a different form of the radiative equilibrium equation to determine the temperature corrections *in the radiative zone*. Equation (1) can be rewritten as

$$\frac{\partial}{\partial \tau_R} \int_0^\infty H_\nu d\nu = 0 , \quad (3)$$

where H_ν is the Eddington flux, or equivalently,

$$H(T, P) = H_0 , \quad (4)$$

where $H = \int_0^\infty H_\nu d\nu$ and H_0 is the surface flux. Linearizing equation (4) with respect to T, we obtain

$$\Delta T = \frac{H_0 - H(T, P)}{\partial H/\partial T|_P} . \quad (5)$$

This expression is used only in the radiative zone (which has a total depth $\Delta\tau_R \ll 1$ for these models) and $\partial H/\partial T|_P$ is evaluated by numerical differentiation. This implicitly takes into account the nonlocal coupling through the radiation field. Equations (3) and (4) are analytically equivalent to equation (1), and equation (5) leads to a continuous $T(P)$ structure in the radiative zone. Numerically, the flux conservation obtained with equation (5) is not as accurate as with equation (1) (if it were, we would find the very same discontinuity). Convergence of these models was judged satisfactory when the radiative equilibrium condition, expressed by equation (1), was satisfied to better than five parts in 10^4. The main drawback of equation (5) is that it converges much more slowly to a final $T(P)$ structure than equation (1). This is reminiscent of the difficulties encountered with the Λ-iteration procedure.

2.4. *The Grid of Models*

We have computed a grid of zero-metallicity model atmospheres over the range $1000 \leq T_{\rm eff} \leq 5000$ K and $3.5 \leq \log g \leq 5.5$ with a helium mass fraction of $Y = 0.25$. This choice of parameters covers VLM main-sequence stars ($M \leq 0.2\ M_\odot$) and their pre–main-sequence evolution as well as the evolution of brown dwarfs with masses down to 0.01 $M_\odot$. Convective energy transport is treated with the mixing-length formalism with a mixing-length parameter of one pressure scale height. The equations of hydrostatic equilibrium, radiative transfer, and radiative equilibrium are solved in the range $-6 \lesssim \log \tau_R \lesssim 2$ which is divided into 50 layers. A few low $T_{\rm eff}$ models show a second radiative zone deep in the atmosphere. We found that increasing the number of layers by about 50% improved the convergence of these models significantly. The radiation field is described with 96 continuum frequency points. A much smoother emergent spectrum is obtained by going to 144 frequency points and the $T(P)$ structure of the atmosphere remains unaffected.

3. ATMOSPHERIC STRUCTURE

The opacity of a low-temperature H/He gas is about two orders of magnitude smaller than that of a gas with a solar admixture of metals. This high transparency of the gas causes zero-metallicity atmospheres to reach high pressures, typically one order of magnitude larger than in the solar metallicity case (see Figs. 15 and 16 of Burrows et al. 1993). The heavy solid lines in Figure 3 show the $T(P)$ structure of a subset of our grid of models with a surface gravity of $\log g = 5$ and effective temperature from 1000 K to 5000 K by steps of 500 K. The corresponding gray atmosphere structures are shown by the thin solid curves. All models shown can be extended to arbitrarily

low pressures once the temperature has reached a constant value (the boundary temperature).

The most striking feature of this figure is the dramatic difference between gray and nongray structures, particularly in the value of the boundary temperature. On the other hand, the $T_{\rm eff}$ = 4500 K and 5000 K gray and nongray models are nearly identical. This is easily explained. For the latter two models, the opacity is dominated by H^- at all depths. The frequency dependence of the H^- opacity is nearly flat in the part of the spectrum where most of the flux emerges and therefore, the opacity is "naturally" gray in these two models. The difference between gray and nongray models increases as $T_{\rm eff}$ is decreased. This is caused by strong departures of the opacity from grayness once H_2 CIA becomes important (Fig. 1). The H_2 CIA forces the top of the convection zone to rise higher in the atmosphere than in the gray case, leading to a lower boundary temperature.

Deep inside the atmosphere, the nongray models are systematically hotter than their gray counterparts. This indicates a higher entropy at large optical depths and that, averaged over the whole structure, the nongray atmosphere is more opaque.

The photosphere ($\tau_{\rm R}$ = 1) of each model is indicated by a triangle in Figure 3. Solid dots indicate transitions between radiative and convective regimes in the atmospheres. All models computed in the grid become convectively unstable at some depth. Interestingly, a few of the low $T_{\rm eff}$ models have a second radiative zone deep in the atmosphere. The 1500 K model shown in Figure 3 becomes convective again at even larger depths. The second radiative zone of the 1000 K model extends at least down to $\tau_{\rm R}$ = 115, and we expect that ultimately it becomes convectively unstable again at a greater depth.

The physics underlying the structure of these atmospheres is illuminated by Figure 4 where the same models are plotted along with entropy contours, or adiabats. The entropy increases toward the lower right part of the figure, i.e., with increasing T and decreasing P. The entropy increases most

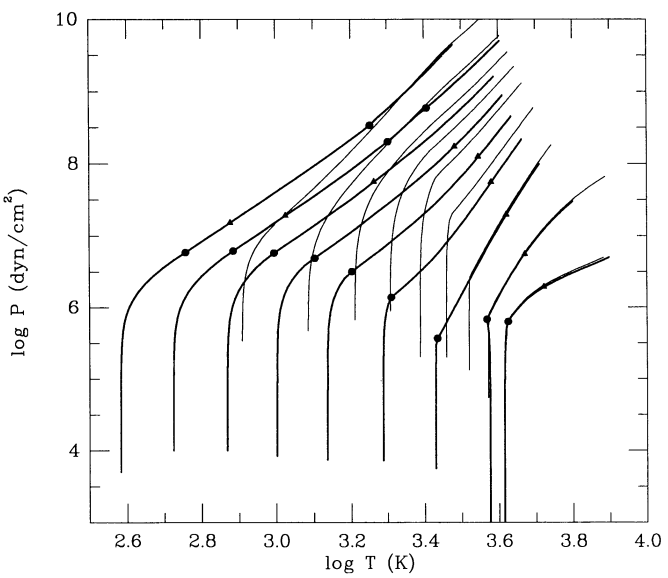

FIG. 3.—Pressure-temperature structure for models with $T_{\rm eff}$ = 1000 K (*left*) to 5000 K (*right*) by steps of 500 K. All models have log g = 5 and Y = 0.25. The thin solid lines show the corresponding *gray* model atmospheres. Triangles indicate the $\tau_{\rm R}$ = 1 level (the photosphere), and solid dots indicate the transitions between radiative and convective zones in the atmosphere.

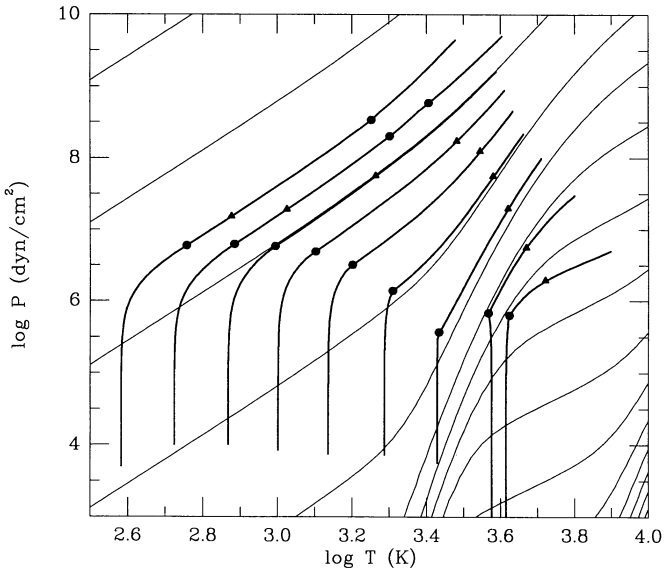

FIG. 4.—Same models as in Fig. 3 plotted on a background of constant specific entropy contours. The entropy increases toward the lower right, most rapidly so in the regions of molecular dissociation (log $T \approx 3.5$) and of ionization of hydrogen (log $T \approx 4$). In the convective zone, all but the two hottest models have a nearly adiabatic structure.

rapidly in the region of molecular dissociation and in the region of ionization of hydrogen at log $T \approx 3.5$ and log $T \approx 4$, respectively. Strikingly, the $T(P)$ structure of the convection zones is nearly adiabatic for all models but the two hottest. Adiabaticity is a clear indication that inside the convection zone, most of the energy is transported by convection and not by radiative losses from the rising mass elements. This is true even though convection occurs in the optically thin part of the atmosphere in all models. The efficiency of convection is measured as the ratio of the energy content of a convective eddy at the time of dissolution to the energy lost by radiation during its lifetime. Within the mixing-length formalism, it is given by

$$\gamma = \frac{\nabla - \nabla'}{\nabla' - \nabla_{\rm ad}}, \qquad (6)$$

where ∇ is the logarithmic temperature gradient (d log T/d log P) in the atmosphere, ∇' is the gradient inside the rising eddy, and $\nabla_{\rm ad}$ is the adiabatic gradient (Mihalas 1978, p. 189). At the top of the convection zone, γ ranges from $\approx 10^2$ to 10^3. Due to a change in the nature of the opacity, it decreases to $\gamma \approx 3$ in the $T_{\rm eff}$ = 5000 K model. Convection is very efficient, and the temperature gradient in the convection zone is close to the adiabatic value in all but the hottest models of our grid. As a consequence, the $T(P)$ structure is insensitive to increases in convective efficiency by raising the value of the mixing-length parameter. However, it is affected by reducing the parameter to uncharacteristically small values ($\lesssim 0.5$).

As can be seen in Figure 4, the convection zone can extend to very high regions in the atmosphere, reaching a maximum in the 4000 K model. In this model, the $T(P)$ profile of the convection zone follows the molecular dissociation region where $\nabla_{\rm ad}$ is smallest, thereby favoring convective instability. This model also shows a discontinuity of the temperature gradient at the transition between radiative and convective regions, a feature of all models where the convection reaches very small values of optical depth. In all models, the temperature is nearly constant

in the radiative zone as long as $\tau_R \ll 1$. The temperature gradient is therefore very small ($\nabla \approx 0$). But as soon as a layer becomes convectively unstable, the high convective efficiency ($\gamma \gg 1$) forces $\nabla \approx \nabla_{ad} \approx 0.1$–$0.4$, causing a sharp bend in the $T(P)$ profile.

4. EMERGENT FLUX DISTRIBUTION AND COLORS

The emergent Eddington flux distributions for the sequence of models shown in Figure 3 are displayed in Figures 5*a*–5*d* (*solid curves*) where they are compared to blackbody energy distributions (*dashed curves*). The $T_{eff} = 5000$ K flux distribution is less instructive and is not shown. Standard photometric bandpasses in the visible and near-infrared are indicated for convenience.

For the hotter models ($T_{eff} \geq 4000$ K), H^- is the main opacity source. It is relatively featureless and frequency-independent and the emergent flux distribution is quite similar to the blackbody function. For lower T_{eff}, the part of the atmo-

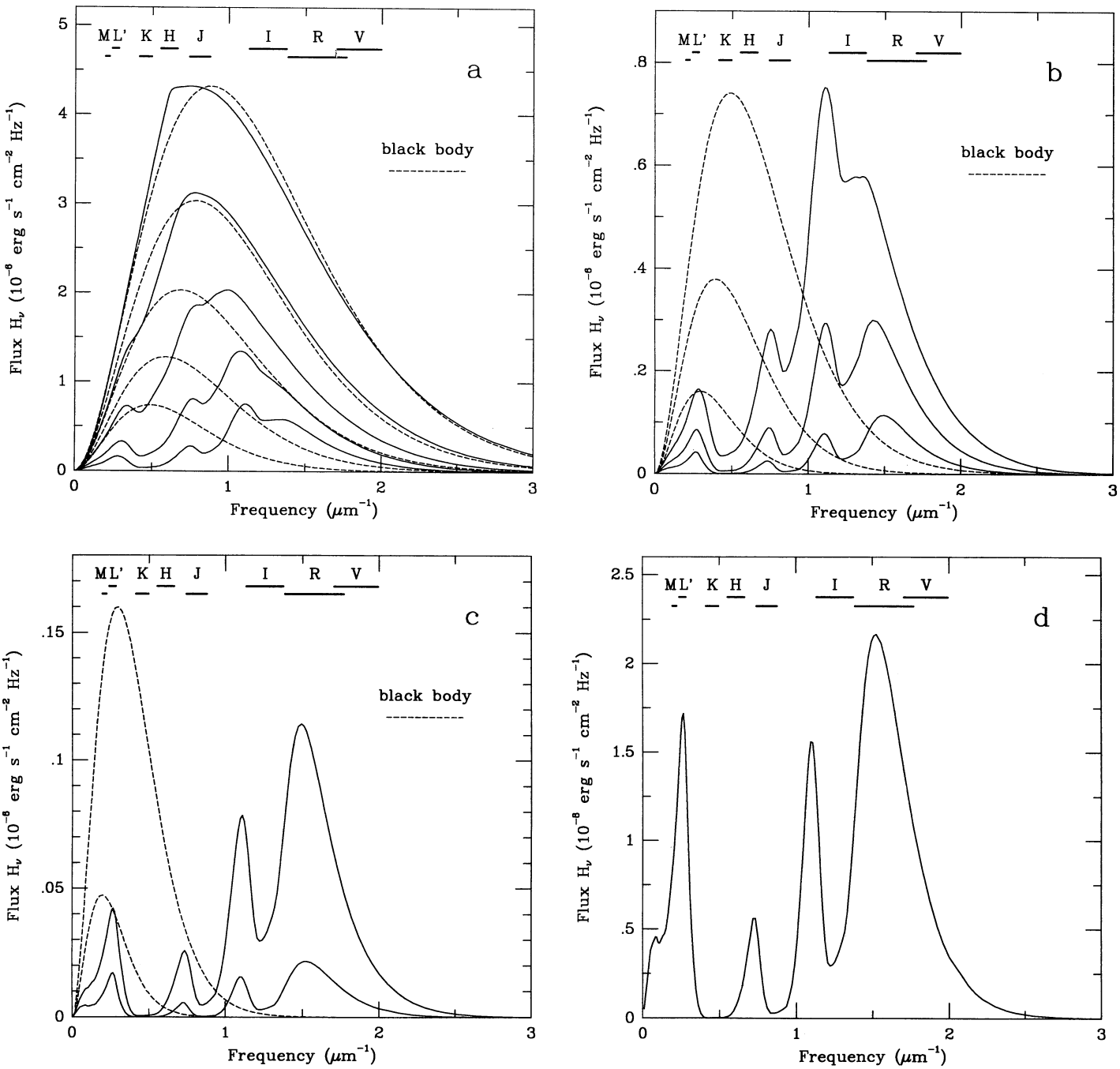

FIG. 5.—Emergent flux distributions for the models presented in Fig. 3. The corresponding blackbody emission is shown by the dashed lines. All models have $\log g = 5$ and $Y = 0.25$. Standard photometric bandpasses (FWHM) are indicated at the top. (*a*) $T_{eff} = 4500$ K (*top*) to 2500 K (*bottom*) by steps of 500 K. (*b*) $T_{eff} = 2500$ K (*top*), 2000 K and 1500 K. (*c*) $T_{eff} = 1500$ K (*top*) and 1000 K. (*d*) $T_{eff} = 1000$ K.

sphere where the spectrum is formed ($\tau_R \lesssim 2$) is cooler and hydrogen is mostly in molecular form. The H_2 CIA now becomes an important source of opacity in the near-infrared ($\nu \lesssim 1.2\ \mu m^{-1}$), where the blackbody flux is important. This strong absorption forces the flux to emerge at higher frequencies, and dramatic deviations from a blackbody spectrum follow (Fig. 5*a*).

The hydrogen molecule absorbs in four major bands, each corresponding to a change in the total vibrational quantum number v of the molecule(s) of $\Delta v = 0$, 1, 2, and 3. Cross sections for higher overtone bands are not available. These broad absorption bands are centered at $\nu \approx 0.16$, 0.4, 0.8, and 1.2 μm^{-1}, respectively. As the temperature is lowered, the collision time between a molecule and its neighbors (H_2, H, He) increases and the bands become narrower and more clearly separated.

For $T_{eff} \leq 2500$ K, the peak emission occurs in the minimum of opacity between H_2 CIA and Rayleigh scattering and remains confined to $1.0 \lesssim \nu \lesssim 1.5\ \mu m^{-1}$ (Figs. 1 and 5*b*–5*d*). Figures 5*a*–5*d* clearly show that as T_{eff} is *decreased*, the peak of emission shifts to the *blue!* This counterintuitive result is a direct consequence of the strong H_2 absorption in the infrared, an absorption which gets stronger as T decreases, just in the frequency range where the blackbody flux at the base of the atmosphere ($\tau_R \gg 1$) is maximum. At the extreme, the $T_{eff} =$ 1000 K spectrum bears no resemblance to either a blackbody or any known stellar spectrum. The H_2 molecule absorbs most strongly in the K photometric bandpass and the emergent spectrum peaks in the I and R bands. The dominant influence of H_2 on the appearance of the spectrum of $Z = 0$ atmospheres underscores the importance of using accurate cross sections for this opacity source.

The emergent spectrum is also sensitive to gravity, as shown by the sequence of 3000 K spectra displayed in Figure 6.

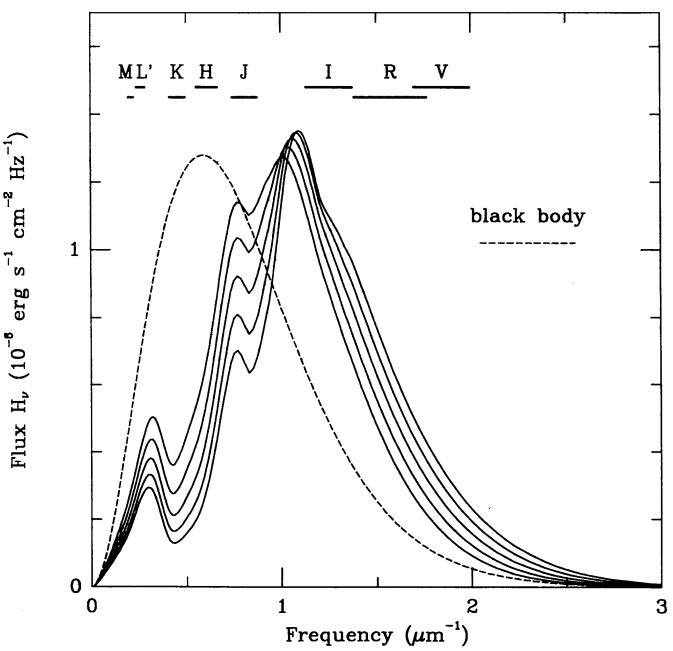

FIG. 6.—Effect of the surface gravity on the emergent flux. All models have $T_{eff} = 3000$ K and $Y = 0.25$. The gravity goes from log $g = 3.5$ (leftmost spectrum) to 5.5 by steps of 0.5. A 3000 K blackbody is shown by the dashed curve and standard photometric bandpasses (FWHM) are indicated at the top.

Surface gravity increases from log $g = 3.5$ to 5.5 (left to right) by steps of 0.5. The pressure in an atmosphere increases roughly linearly with the gravity. The absorption coefficient of the H_2 CIA per molecule, being a *collisional* process, is proportional to the total pressure P. It follows that H_2 absorption becomes stronger with increasing g, pushing the emergent flux toward higher frequencies, as seen in Figure 6. The effect on the emergent flux of an increase in g is qualitatively similar to that of a decrease in T_{eff}.

Using the filter transmission curves and absolute calibration given in Bessell (1990) and Bessell & Brett (1988), we have computed colors and the V bolometric correction for all models in our grid (Table 1). A large set of color-color diagrams can be generated from this table: two are shown in Figure 7. In these diagrams, each model from Table 1 is represented by a diamond. Solid lines connect models with the same T_{eff}, and an open diamond indicates the log $g = 3.5$ model of each sequence. A heavy dashed line shows the $Z = 0$ main sequence (see below) from 0.092 $M_\odot$ (*open circle*) to 0.2 $M_\odot$.

Because of the jagged nature of the emergent flux distribution, it is difficult to interpret physically (e.g., in terms of T_{eff} and g) the trends seen in the colors. The $J-K$ versus $R-I$ diagram offers a fairly good separation of T_{eff} and g. Interestingly, both colors become independent of gravity and effective temperature at high T_{eff}. Table 1 indicates that $V-R$ and $V-I$ are good temperature indicators for $T_{eff} \geq 4000$ K. The main sequence is found in the high-g high T_{eff} part of the diagram. All other models correspond to pre–main-sequence evolution or brown dwarfs (see below).

By contrast, all models form a single sequence in the $J-H$ versus $H-K$ diagram: it is impossible to distinguish variations in g from variations in T_{eff}. This reflects our earlier observation that changes in g and T_{eff} have a qualitatively similar effect on the energy distribution.

Two $T_{eff} = 3000$ K, log $g = 5$ models are shown in Figure 8: Our $Z = 0$ model and a $[M/H] = -3$ ($Z \approx 0.001\ Z_\odot$) model from Allard (1993). The latter model uses the same H_2 CIA cross sections, but also includes about 3000 atomic lines as well as molecular absorption mainly by TiO, VO, H_2O, CO, CaH, and FeH. Even such a small amount of metals generates numerous absorption features in the visible part of the spectrum. While the two spectra share a similarity in overall shape, these new absorption features force the flux back toward the near-infrared, resulting in a redder spectrum, somewhat closer to the blackbody flux distribution. It is clear however, that for $Z/Z_\odot = 0.001$, the near-infrared part of the spectrum is dominated by H_2 absorption, and not by the H_2O and CO features observed in higher metallicity stars. Without a sequence of synthetic spectra of decreasing metallicity, it is difficult to estimate the minimum metallicity which will cause a significant departure from the $Z = 0$ flux distribution. Figure 8 suggests that this value is below $\approx 10^{-4}\ Z_\odot$, lower than the values determined for the most extreme metal-poor stars known. Nevertheless, the $Z = 0$ atmospheres and emergent flux distributions can be used to constrain and interpret observations once they are coupled with interior models.

5. OF ATMOSPHERES AND INTERIORS

For most of the last decade, increasingly sensitive infrared detectors have fueled a great interest in observational and theoretical studies of the low-mass end of the main sequence and of the substellar brown dwarfs. While the modeling of the atmospheres of late M dwarfs and brown dwarfs is just gaining

TABLE 1

COLORS AND BOLOMETRIC CORRECTIONS FOR $Z = 0$ ATMOSPHERES[a,b]

$T_{\rm eff}$ (K)	log g (cm s^{-2})	$V-R$	$V-I$	$V-J$	$V-H$	$V-K$	$V-L'$	$V-M$	BC(V)
1000.....	3.50	1.21	1.49	1.00	1.04	−1.90	5.14	5.14	−0.71
1000.....	4.00	1.10	0.96	0.27	0.35	−2.81	4.59	4.57	−0.30
1000.....	4.50	1.00	0.53	−0.39	−0.32	−3.76	4.10	4.07	0.00
1000.....	5.00	0.85	−0.02	−1.04	−0.95	−4.63	3.64	3.60	0.29
1000.....	5.50	0.92	−0.26	−1.34	−1.23	−5.07	3.47	3.42	0.36
1500.....	3.50	1.44	2.20	1.65	1.45	−0.14	4.55	4.61	−0.93
1500.....	4.00	1.30	1.72	0.96	0.78	−1.00	4.01	4.06	−0.53
1500.....	4.50	1.13	1.12	0.15	0.00	−1.99	3.41	3.46	−0.10
1500.....	5.00	0.96	0.54	−0.50	−0.62	−2.81	2.96	2.99	0.21
1500.....	5.50	0.78	−0.06	−1.18	−1.26	−3.72	2.49	2.51	0.49
2000.....	3.50	1.46	2.54	2.27	1.92	1.06	4.24	4.32	−1.15
2000.....	4.00	1.32	2.15	1.58	1.24	0.27	3.70	3.78	−0.74
2000.....	4.50	1.18	1.74	0.93	0.61	−0.48	3.21	3.29	−0.39
2000.....	5.00	1.05	1.31	0.34	0.03	−1.18	2.79	2.86	−0.09
2000.....	5.50	0.91	0.88	−0.22	−0.49	−1.84	2.39	2.46	0.17
2500.....	3.50	1.33	2.47	2.73	2.42	1.95	4.01	4.11	−1.22
2500.....	4.00	1.22	2.22	2.18	1.82	1.29	3.55	3.65	−0.88
2500.....	4.50	1.12	1.97	1.66	1.27	0.68	3.13	3.23	−0.60
2500.....	5.00	1.02	1.72	1.18	0.78	0.13	2.77	2.87	−0.35
2500.....	5.50	0.93	1.47	0.75	0.35	−0.36	2.46	2.55	−0.15
3000.....	3.50	1.14	2.17	2.91	2.86	2.73	3.89	3.99	−1.19
3000.....	4.00	1.05	2.02	2.56	2.42	2.20	3.52	3.61	−0.94
3000.....	4.50	0.98	1.88	2.22	1.99	1.70	3.18	3.27	−0.73
3000.....	5.00	0.92	1.76	1.89	1.59	1.24	2.87	2.97	−0.55
3000.....	5.50	0.87	1.64	1.57	1.21	0.82	2.60	2.70	−0.40
3500.....	3.50	0.92	1.79	2.74	2.97	3.08	3.67	3.78	−1.02
3500.....	4.00	0.88	1.72	2.60	2.74	2.82	3.47	3.58	−0.90
3500.....	4.50	0.84	1.66	2.44	2.50	2.52	3.26	3.36	−0.78
3500.....	5.00	0.81	1.60	2.27	2.25	2.20	3.04	3.14	−0.67
3500.....	5.50	0.78	1.54	2.09	1.98	1.85	2.81	2.91	−0.56
4000.....	3.50	0.74	1.48	2.35	2.82	2.99	3.32	3.41	−0.78
4000.....	4.00	0.72	1.45	2.30	2.72	2.84	3.22	3.31	−0.73
4000.....	4.50	0.71	1.42	2.25	2.60	2.70	3.12	3.21	−0.68
4000.....	5.00	0.70	1.40	2.20	2.48	2.55	3.01	3.10	−0.63
4000.....	5.50	0.68	1.37	2.14	2.34	2.39	2.88	2.98	−0.58
4500.....	3.50	0.58	1.18	1.91	2.42	2.58	2.74	2.79	−0.50
4500.....	4.00	0.59	1.19	1.92	2.41	2.57	2.75	2.81	−0.51
4500.....	4.50	0.59	1.19	1.91	2.36	2.53	2.73	2.79	−0.49
4500.....	5.00	0.59	1.19	1.90	2.33	2.49	2.71	2.78	−0.48
4500.....	5.50	0.59	1.19	1.88	2.27	2.41	2.67	2.74	−0.47

[a] We adopted the filter transmission curves and the absolute calibration of Bessell & Brett 1988 and Bessell 1990.
[b] $Y = 0.25$.

momentum, their evolution has been studied by several groups (see the reviews by Stevenson 1991, and Burrows & Liebert 1993).

The lives of VLM stars and brown dwarfs present a relatively simple problem of stellar evolution. All of these objects have fully convective interiors and are essentially adiabatic. The evolutionary timescale is almost exclusively controlled by the atmosphere which constitutes a very thin, insulating surface layer. The ability of the atmosphere to let energy escape to space depends strongly on the opacity of the gas, which is a steep function of metallicity. The atmosphere, seen as a surface boundary condition (BC) to the equations of stellar structure and evolution, therefore plays a very important role in this type of object. Nevertheless, nearly all evolutionary calculations rely on a crude description of the atmosphere as a boundary condition. The most common approach is to perform some form of integration of the equation of hydrostatic equilibrium:

$$\frac{dP}{d\tau_{\rm R}} = \frac{g}{\kappa_{\rm R}}, \tag{7}$$

assuming a gray $T(\tau_{\rm R})$ structure, down to the level where the atmosphere becomes convectively unstable. The crudest approach is to do a one-step integration of equation (7) and solve for T and P such that

$$\frac{P}{\tau_{\rm R}} = \frac{g}{\kappa_{\rm R}} \tag{8}$$

at the "surface" of the star. Even for gray atmospheres, such approaches are very approximate because they do not consider the problem of radiative transfer.

Burrows et al. (1993) presented the evolution of VLM stars and brown dwarfs of both zero and solar metallicities where the surface BC was obtained with gray atmospheres. These atmospheres treated the problem of radiative transfer explicitly and self-consistently with energy transport by convection. The BC is then expressed as a relation between the entropy of the interior adiabat S (obtained at a level where the atmospheric structure becomes adiabatic) and the atmospheric parameters: $S(T_{\rm eff}, g, Y, Z)$. The grid of nongray model atmospheres of zero-metallicity presented here provides us with a new and

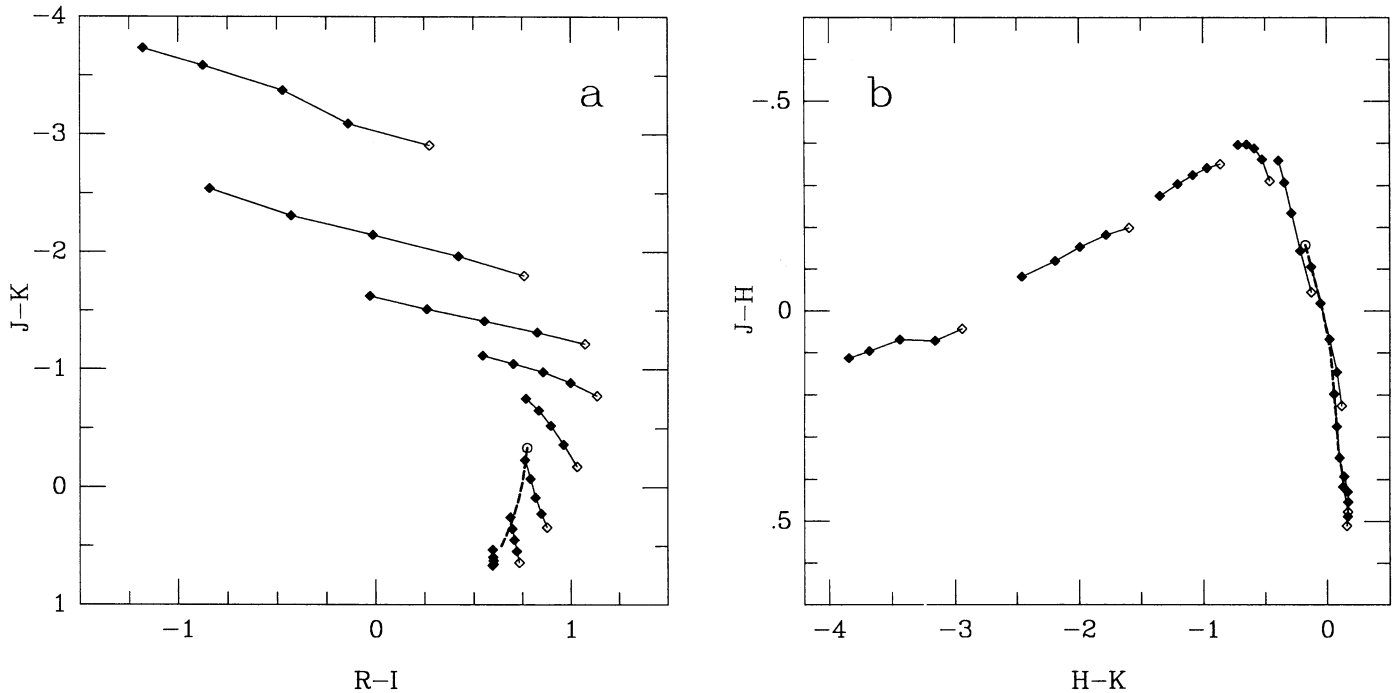

FIG. 7.—Color-color diagrams for all the models of Table 1. Solid lines connect models with the same $T_{\rm eff}$ but with different surface gravities. Each model is indicated by a diamond; the log g = 3.5 models of each $T_{\rm eff}$ sequence is shown by an open diamond. The heavy dashed line marks the locus of the Z = 0 main sequence for masses below 0.2 $M_\odot$. The minimum main-sequence mass (0.092 $M_\odot$) is shown by an open circle. (*a*) In the $(J-K)$ vs. $(R-I)$ diagram, the upper curve corresponds to $T_{\rm eff}$ = 1000 K. (*b*) In the $(J-H)$ vs. $(H-K)$ diagram, the $T_{\rm eff}$ = 1000 K model sequence is at the left.

accurate surface BC for zero-metallicity stars. Figure 9 compares the gray and the nongray surface BC $S(T_{\rm eff}, g)$ with Y = 0.25 and Z = 0. Note that the entropies indicated for the

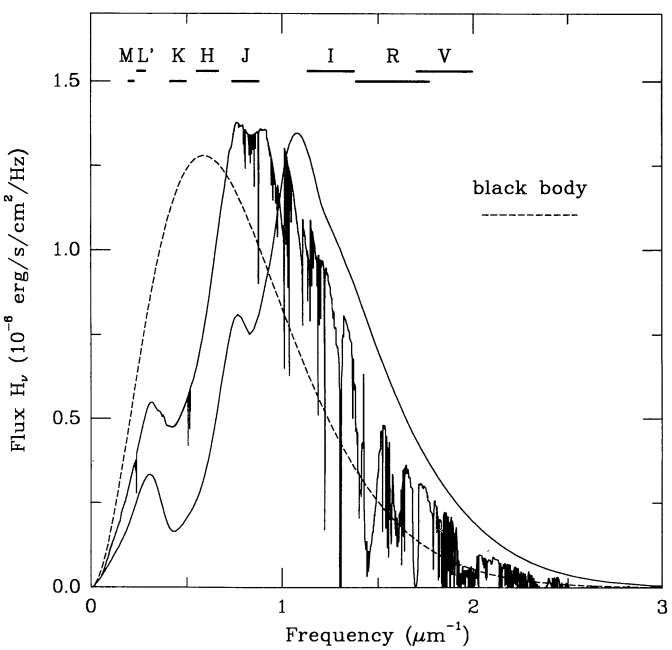

FIG. 8.—Comparison between $T_{\rm eff}$ = 3000 K, log g = 5 synthetic spectra of zero metallicity and with a small but finite metallicity of $[M/H] = -3$ (Allard 1993). The flux distribution of a 3000 K blackbody is represented by the dashed curve. Standard photometric bandpasses (FWHM) are indicated at the top.

1000 K nongray models are strictly upper values because the integration of the atmosphere ends in the second radiative zone (which is not adiabatic), as discussed in § 3. The largest differences are found at high gravity and for effective temperatures in the ≈2000 K to 3500 K range, parameters characteristic of relatively young and massive brown dwarfs. The effect on the location of the Z = 0 main-sequence stars, which are hotter, should be more modest but still significant.

We have recomputed the evolution of Z = 0 objects in the 0.01 to 0.2 $M_\odot$ range (model Z of Burrows et al. 1993) using the new, nongray surface boundary condition. Moderate quantitative differences result from this new calculation, although it is qualitatively identical to model Z. The results are summarized in Figure 10 which shows evolutionary tracks in the ($T_{\rm eff}$, log g) plane. Open circles show the grid of nongray model atmospheres. The evolution proceeds from the upper left toward the lower right part of the diagram, in a fashion similar to the evolution in an Hertzsprung-Russell diagram. Diamonds along each track indicate ages of 10^6, 10^7, 10^8, 10^9, and 10^{10} yr, respectively. From left to right, the tracks correspond to masses of 0.2, 0.15, 0.1, 0.092, 0.09, 0.08, 0.07, 0.06, 0.05, 0.04, 0.03, 0.02, and 0.01 $M_\odot$. The first four stabilize on the main sequence after ≈10^9 yr. The other objects are brown dwarfs.

Physical and photometric characteristics of the low-mass end of the Z = 0 main sequence are given in Table 2 and displayed in Figure 7. The minimum mass for the Z = 0 main sequence obtained here, 0.092 $M_\odot$, is the lowest reported so far. It can be demonstrated analytically that the minimum main-sequence mass decreases when the atmospheric opacity is increased (Burrows & Liebert 1993). Using opacities which did not include the H_2 CIA and an approximate gray surface BC, D'Antona (1987) obtained a value of 0.115 $M_\odot$. With updated opacities which include the H_2 CIA, Burrows et al. (1993)

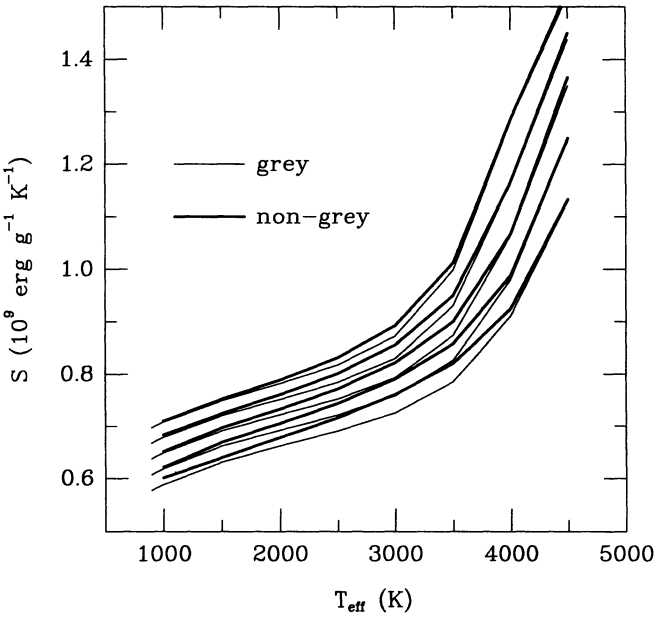

FIG. 9.—The surface boundary condition used for evolutionary calculations shown as $S(T_{eff}, g)$, where S is the entropy at the base of the atmosphere. Each pair of curves corresponds to a value of the surface gravity, ranging from $\log g = 3.5$ (*top*) to 5.5 by steps of 0.5. The $S(T_{eff}, g)$ relation for both gray and nongray model atmospheres is shown.

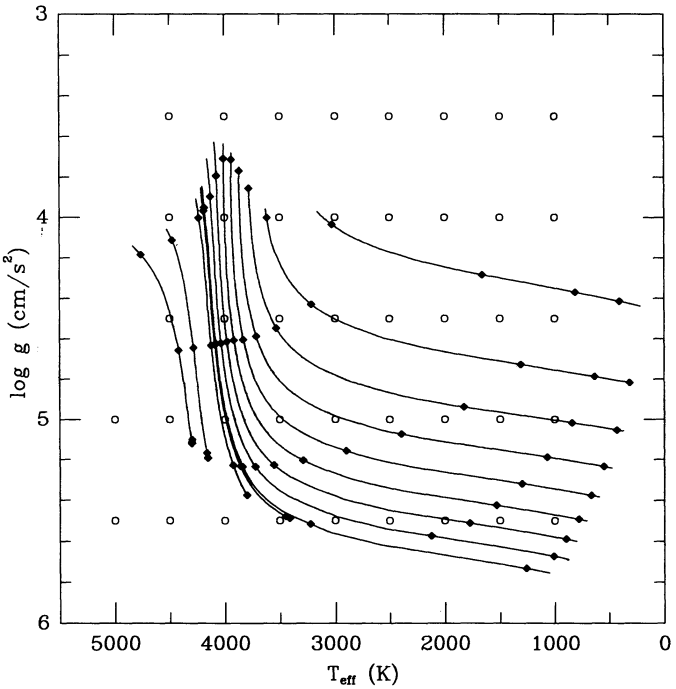

FIG. 10.—Evolution of VLM stars and brown dwarfs of zero metallicity in the ($\log g$, T_{eff}) plane. Starting from the upper right, the mass for each evolutionary track is 0.01, 0.02, 0.03, 0.04, 0.05, 0.06, 0.07, 0.08, 0.09, 0.092, 0.1, 0.15, and 0.2 $M_\odot$, respectively. The evolution proceeds from the upper left toward the lower right part of the diagram, with diamonds indicating ages of 10^6, 10^7, 10^8, 10^9, and 10^{10} yr, respectively. Open circles show the grid of computed nongray model atmospheres.

revised this value downward to 0.094 $M_\odot$. This arises from the substantial increase in opacity due to H_2 absorption. By using nongray atmospheres as a surface BC, which effectively increases the average atmospheric opacity compared to the otherwise identical gray case (see § 3), the value is further reduced to 0.092 $M_\odot$. As expected, the properties of the low-mass end of the main sequence computed with a nongray surface boundary condition are close to the gray case.

If we neglect the minute amounts of elements heavier than helium produced during the primordial nucleosynthesis, zero-metallicity models describe the very first generation of stars, the so-called Population III stars. The mass function of this stellar population could extend down to the VLM range since collapsing clouds can fragment into low mass stars even in the absence of heavy elements (Palla, Salpeter, & Stahler 1983). Model Z of Burrows et al. (1993) shows that $Z = 0$ brown dwarfs are all extremely faint and essentially undetectable after 10^{10} yr of cooling, with $L/L_\odot \lesssim 10^{-6}$. This is a consequence of their transparent atmospheres which allow energy to escape more freely. On the other hand, if VLM stars of zero metallicity formed in the distant past, they have remained virtually unchanged to this day. Figures 6 and 18 of Burrows et al. (1993) show that the $Z = 0$ main sequence is slightly more luminous than its $Z = Z_\odot$ counterpart, for which numerous examples have been discovered in the solar neighborhood. Table 2 shows that they are not especially faint and Figure 5*a* indicates that they would be brightest in the *I*, *J*, and *H* bandpasses.

This is the first accurate calculation of the low-mass end of the $Z = 0$ main-sequence properties. Since it represents the extreme case of low metallicity, it provides a rigid boundary in the Hertzsprung-Russell diagram which can assist in the interpretation of data, as we now show.

Figure 11 shows a sample of 354 low-luminosity stars from the US Naval Observatory stellar parallax program, as compiled by Monet et al. (1992). Besides illustrating the low-mass end of the main sequence beautifully, this figure also shows a

TABLE 2

PHOTOMETRIC PROPERTIES OF THE LOW-MASS END OF THE $Z = 0$ MAIN SEQUENCE[a,b]

M ($M_\odot$)	T_{eff} (K)	$\log g$ (cm s^{-2})	M_{bol}[c]	M_V	$V-R$	$V-I$	$V-J$	$V-H$	$V-K$	$V-L$	$V-M$
0.200.....	4298	5.12	9.46	10.01	0.63	1.27	2.02	2.41	2.53	2.85	2.93
0.150.....	4155	5.19	10.10	10.68	0.66	1.33	2.10	2.43	2.51	2.91	2.99
0.125.....	4041	5.25	10.58	11.18	0.68	1.37	2.15	2.41	2.48	2.93	3.02
0.100.....	3796	5.38	11.38	11.99	0.73	1.46	2.20	2.30	2.32	2.93	3.03
0.095.....	3643	5.43	11.75	12.35	0.76	1.51	2.17	2.17	2.13	2.89	2.99
0.092.....	3410	5.49	12.22	12.76	0.80	1.57	2.03	1.87	1.69	2.78	2.87

[a] We adopted the filter transmission curves and the absolute calibration of Bessell & Brett 1988 and Bessell 1990.
[b] $Y = 0.25$.
[c] Using $M_{bol}(\odot) = 4.72$.

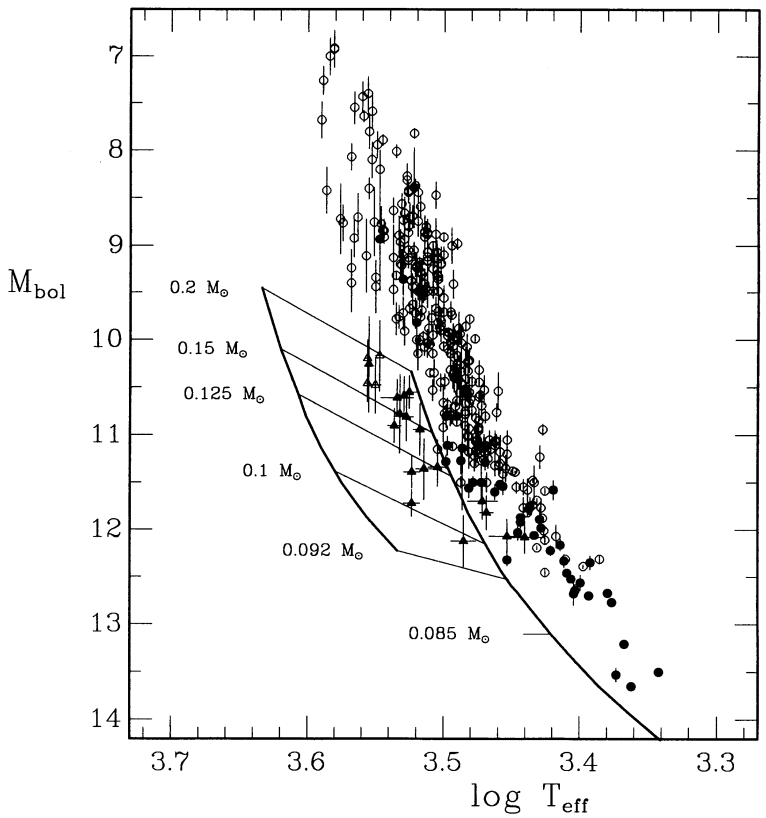

FIG. 11.—Hertzsprung-Russell diagram comparing the observations reported in Monet et al. (1992) with our calculations. Members of the observed extreme subdwarf sequence are indicated by triangles. The solid curve on the left shows the $Z = 0$ main sequence computed with the nongray surface boundary condition of Fig. 8. The $Z = Z_\odot$ main sequence computed with a *gray* surface boundary condition by Burrows et al. (1993) is shown to the right. Thin lines connect models of equal masses in each sequence (see text). Adapted from Fig. 14 of Monet et al. (1992).

well-defined subdwarf sequence to the left of the main sequence (*triangles*). All of these subdwarfs have very large space velocities which clearly identify them as part of the halo population. Further details are given in Monet et al. (1992). Superposed on the data are the $Z = Z_\odot$ main sequence of Burrows et al. (1993), which uses a gray surface boundary condition, and the present $Z = 0$ main-sequence calculation. Thin solid lines connect models of equal masses. The low-mass end of the $Z = Z_\odot$ main sequence is outside the figure, at $M = 0.077\ M_\odot$, $\log T_{eff} = 3.24$, and $M_{bol} = 15.25$.

The large discrepancy between the location of the observed and theoretical main sequences was noticed several years ago. This disagreement, where the observed main sequence is cooler than predicted from the models, is found in almost every such comparison, regardless of the source of data or of the models used in the comparison (Burrows & Liebert 1993 and references therein). It has now become clear that the conversions between photometric colors and T_{eff}, which until recently were all based on some form of blackbody fitting, systematically underestimate T_{eff} for VLM stars. In the first attempt to resolve this unsatisfactory situation, Kirkpatrick et al. (1993) determined T_{eff} by fitting near-infrared *spectra* with the synthetic spectra of Allard (1990). They obtained luminosities and temperatures which agree very well with theoretical predictions, confirming the suspicion that color temperatures underestimate T_{eff}. Jones et al. (1994) reached the same conclusion in a complementary study.

In view of the previous remarks, if we slide the data points of Figure 11 along the T_{eff} axis to match the observed and the computed $Z = Z_\odot$ main sequences, we find that the computed $Z = 0$ main sequence nicely delimits the extent of the extreme subdwarf sequence. We have implicitly assumed that the degree to which the effective temperature of the observed stars is underestimated does not depend on their metallicity. This is very difficult to verify since Monet et al. (1992) use different T_{eff} versus $(V-I)$ calibrations for the dwarf and subdwarf sequences. Only T_{eff} and M_{bol} based on fits of observed spectra will resolve this issue. This exercise of fitting theory and observations suggests that some of the stars in this sequence have metallicities much lower than the $0.02\ Z_\odot$ value adopted by Monet et al. (1992). The survey of Population II stars in the spheroid of the Galaxy by Richer & Fahlman (1992) also supports this contention. Moreover spotty spectroscopic data for some of the extreme subdwarfs of Figure 11 show a near absence of TiO absorption bands (Monet et al. 1992). The $[M/H] = -3$ synthetic spectrum displayed in Figure 8, however, shows TiO absorption near $\nu = 1.27$ and $1.4\ \mu m^{-1}$, providing additional evidence that there are extremely low metallicity stars among this sequence. We can firmly state that regardless of the method used to obtain T_{eff} and M_{bol}, no star should lie to the left of the $Z = 0$ main sequence shown in Figure 11 (with an allowance for a weak dependence on Y).

6. CONCLUSIONS

This is the first set of detailed zero-metallicity atmosphere models for cool stars. The substantial improvement in the H_2 CIA cross sections has been crucial for this work as it is the

least well understood of the three important opacity sources relevant for VLM stars and brown dwarfs of extremely low metallicity. The $Z = 0$ atmospheres are dense and all become convective in the optically thin layers. The emergent spectrum deviates strongly from a blackbody and in the more extreme case of low effective temperature, it does not resemble any known stellar spectrum. It follows that effective temperatures based on blackbody fits to broad-band photometry of extremely low-metallicity stars are unreliable. Only spectroscopic data fitted with synthetic spectra can provide the accuracy required to understand these objects.

The evolution of $Z = 0$ VLM stars and brown dwarfs was recomputed using the nongray atmosphere as a surface boundary condition. The minimum mass for hydrogen burning is now established at 0.092 $M_\odot$ and the computed photometric properties of the main sequence up to 0.2 $M_\odot$ provide a reliable basis to compare theoretical models directly with observations. The $Z = 0$ main sequence represents the extreme limit of low-metallicity and as such, it forms a boundary in the Hertzsprung-Russell diagram which is useful to interpret data on low-metallicity stars. VLM stars spend more than a Hubble time on the main sequence. If the first generation of stars included VLM stars, they should still be visible with today's instrumentation. Population III brown dwarfs, on the other hand, would have cooled to luminosities well below the current detectability limit.

We are most grateful to P. Lenzuni for providing us with cross sections for the collision-induced absorption by H_2. We also thank F. Allard for sending us results prior to publication and C. C. Dahn for kindly providing an original of a published figure. This research was supported in part by NSERC of Canada, by the fund FCAR (Québec), by NSF grants AST 89-10780 and AST 89-14346, by a grant to George H. Rieke from the NASA Origins of the Solar System program (NAGW-2606), and by NASA grant HF-1051.01-93A from the Space Telescope Science Institute, which is operated by the Association of Universities for Research in Astronomy, Inc., under NASA contract NAS 5-26555.

REFERENCES

Alcock, C., et al. 1993, Nature, 365, 621
Allard, F. 1990, Ph.D. thesis, Ruprecht Karls Univ. Heidelberg
———. 1993, private communication
Aubourg, E., et al. 1993, Nature, 365, 623
Bergeron, P. 1988, Ph.D. thesis, Univ. Montréal
Bergeron, P., Wesemael, F., & Fontaine, G. 1991, ApJ, 367, 253
Bessell, M. S. 1990, PASP, 102, 1181
Bessell, M. S., & Brett, J. M. 1988, PASP, 100, 1134
Borysow, A. 1993, private communication
Borysow, A., & Frommhold, L. 1989, ApJ, 341, 549
———. 1990, ApJ, 348, L41
Borysow, A., Frommhold, L., & Moraldi, M. 1989, ApJ, 336, 495
Burrows, A., Hubbard, W. B., Saumon, D., & Lunine, J. I. 1993, ApJ, 406, 158
Burrows, A., & Liebert, J. 1993, Rev. Mod. Phys., 65, 301
Canuto, V. M., & Mazzitelli, I. 1992, ApJ, 389, 724
Chandra, S., Gaur, V. P., & Pande, M. C. 1991, J. Quant. Spectrosc. Rad. Transfer, 45, 57
D'Antona, F. 1987, ApJ, 320, 653
Huber, K. P., & Herzberg, G. 1979, Molecular Spectra and Molecular Structure. IV. Constants of Diatomic Molecules (Princeton: Van Nostrand)
Jones, H. R. A., Longmore, A. J., Jameson, R. F., & Mountain, C. M. 1994, in preparation
Kirkpatrick, J. D., Kelly, D. M., Rieke, G. H., Liebert, J., Allard, F., & Wehrse, R. 1993, ApJ, 402, 643
Kui, R. 1991, Ph.D. thesis, Australian National Univ.
Leggett, S. K. 1992, ApJS, 82, 351
Lenzuni, P., Chernoff, D. F., & Salpeter, E. E. 1991, ApJS, 76, 759
Linsky, J. L. 1969, ApJ, 156, 989
Lunine, J. I., Saumon, D., Hubbard, W. B., & Burrows, A. 1993, in Proc. Internat. Conf. Physics of Strongly Coupled Plasmas, ed. H. M. Van Horn & S. Ichimaru (Rochester, N.Y.: Univ. of Rochester Press), p. 137
Lydon, T. J., Fox, P. A., Sofia, S. 1992, ApJ, 397, 701
Mihalas, D. 1978, Stellar Atmospheres (2d ed.; San Francisco: Freeman)
Monet, D. G., Dahn, C. C., Vrba, F. J., Harris, H. C., Pier, J. R., Luginbuhl, C. B., & Ables, H. D. 1992, AJ, 103, 638
Palla, F., Salpeter, E. E., & Stahler, S. W. 1983, ApJ, 271, 632
Patch, R. W. 1971, J. Quant. Spectrosc. Rad. Transf., 11, 1331
Richer, H. B., & Fahlman, G. G. 1992, Nature, 358, 383
Saumon, D., & Chabrier, G. 1992, Phys. Rev. A, 46, 2084
Stevenson, D. J. 1991, ARA&A, 29, 163